Sustainable Lead Management in Halide Perovskite Solar Cells

So Yeon Park,[†a,b] Ji-Sang Park,[†c] Byeong Jo Kim,[a,d] Hyemin Lee,[e] Aron Walsh,[f,g] Kai Zhu,[h] Dong Hoe Kim*[e] & Hyun Suk Jung*[a]

[a] School of Advanced Materials Science & Engineering, Sungkyunkwan University, Suwon 16419, Republic of Korea
[b] Nanomechanical Systems Research Division, Korea Institute of Machinery and Materials, Daejeon, 34103, Republic of Korea
[c] Department of Physics, Kyungpook National University, Daegu, 41566, Republic of Korea
[d] Department of Chemistry-Ångström Laboratory, Physical Chemistry, Uppsala University, Box 523, SE 751 20 Uppsala, Sweden
[e] Department of Nanotechnology and Advanced Materials Engineering, Sejong University, Seoul 05006, Republic of Korea
[f] Thomas Young Centre and Department of Materials, Imperial College London, London SW72AZ, UK
[g] Department of Materials Science and Engineering, Yonsei University, Seoul 07322, Republic of Korea
[h] Chemistry and Nanoscience Center, National Renewable Energy Laboratory, Golden, Colorado 80401, USA

[†] S.Y.P and J.P. contributed equally to this work.
[*] Corresponding authors.
Correspondence: hsjung1@skku.edu (H.S. Jung), donghoe.k@sejong.ac.kr (D.H. Kim)

Abstract

Despite the rapid development of perovskite solar cells (PSCs) toward commercialization, the toxic Pb ions in PSCs pose a potential threat to the environment, health, and safety. Managing Pb via recycling represents a promising approach to mitigating its toxicity. However, managing Pb from commonly used organic solvents has been challenging due to the lack of suitable Pb adsorbents. Here, we report a novel adsorbent for both separation and recovery of Pb from PSC pollutants. The synthesized Fe-incorporated hydroxyapatite possesses a strongly negatively charged surface that improves electrostatic interaction through surface-charge delocalization, thus leading to enhanced Pb adsorption. We demonstrate the feasibility of a complete Pb management process, including the purification of Pb-containing non-aqueous solvents below 15

ppb, a level compliant with the standards of the U.S. Environmental Protection Agency, as well as recycling of 99.97% Pb ions by forming PbI_2.

Lead halide perovskite, containing organic or inorganic cations, lead ions and halide ions in the perovskite structure, shows superior photovoltaic (PV) performance and stability, as well as immense potential for being scaled up, which makes it the most promising emerging PV technology.[1-6] However, potentially long-term risks may be incurred due to treatment of Pb-containing nonaqueous waste during fabrication as well as the continuous exposure to Pb from waste or the device itself. Therefore, the environmental, health, and safety (EHS) effects of the materials and processes involved could be a major concern in perovskite solar cell (PSC) commercialization.[7-11] The PV industry has an existing exemption to the Restriction of Hazardous Substances Directive (RoHS)—namely, CdTe solar cells. These cells have been commercialized despite the hazardous element Cd, because Cd is controlled through a meticulous management and recycling program—from production to disposal of the CdTe.[7,10] To follow in CdTe's path, lead halide PSCs must track and recycle Pb during all phases of a module's lifetime.

Several approaches have been considered for managing Pb from an aqueous solution, such as precipitation,[12] membrane filtration,[13] and adsorption using adsorbent;[14,15] but none has been established yet for the nonaqueous pollutant. We want to recover a Pb-containing nonaqueous liquid pollutant, generated while fabricating PSCs, in an industrial application at below-ppm levels and do so cost effectively. The adsorption approach is one of the best candidates because it can enhance the reactivity with Pb, making it easy to retrieve from the solution after adsorption; and it can be scaled up for commercialization.[15]

Various strategies exist to improve adsorption capability of adsorbents, which could adsorb atoms, ions or molecules from gas, liquid, or salt-dissolved solution on their surface, such as increased surface area, chemical activation of the absorption surface, and formation of a hybrid composite. Of these, hybrid composites have been explored most widely because they efficiently incorporate all the advantages mentioned.[15-19] However, hybrid composites have a major disadvantage—the trade-off between functionality and decreasing the density of active surface sites due to unequal absorption properties of each material.

A strategy to address this trade-off is to strengthen the negative surface and enhance the electrostatic interaction via charge delocalization, using doping by metallic elements (e.g., Fe

and Mg) on the active surface sites in hybrid composites. Among various negatively charged Pb adsorbents, such as MnO_2 or zeolites, or hydroxyapatite ($Ca_{10}(PO_4)_6(OH)_2$, HAP),[14-15,20-21] has many advantages over its competitors. HAP is inexpensive and bio- and environment-friendly, and it has Earth-abundant components and easily controllable morphology and size. But in particular, it has lattice-expansion flexibility for a broad range of doping, and it has a malleable surface charge via doping.[20-23] These two properties are especially significant because they can readily control the surface charge of HAPs via the various choices of dopants.

In this paper, we report on sustainable Pb management, during the entire fabrication of PSCs, via the design of an Fe-decorated HAP hollow composite (HAP/Fe). HAP/Fe serves two critical functions: 1) it modifies the surface charge to enhance Pb adsorption capacity, and 2) it assigns magnetism for easy collection of Pb-adsorbed HAP/Fe from solvents. The purified polar solvent dropped below 15 ppb of Pb, meeting the standards of the U.S. Environmental Protection Agency (EPA). Using the solubility difference between HAP/Fe and Pb^{2+} ions under different pH values, we recycled Pb wastes as PbI_2 with a high recycling yield of 99.97%. The demonstrated devices using only recycled components (e.g., recycled TiO_2/FTO substrate and PbI_2) confirmed the feasibility of sustainable fabrication of PSCs by showing comparable performance to that of fresh devices.

Synthesis of Fe decorated HAP

HAP/Fe hollow composites were synthesized via a three-step process, as illustrated in Fig. 1a. First, three-dimensional (3D) branched HAP hollow-structured particles were synthesized via a Kirkendall effect ion-exchange method based on $CaCO_3$ spheres.[24,25] The hollow interior of HAP is observed in a field-emission scanning electron microscope (FE-SEM) image (the first step in Fig. 1a). More than 1 μm in size and hollow, its nanorod building blocks, which are grown along the c-axis, are revealed in high-resolution transmission electron microscope (HR-TEM) images (Supplementary Fig. 1a and b). Further, the low-magnification FE-SEM image in Supplementary Fig. S1c shows its morphological homogeneity. Supplementary Fig. 2 and Table 1 illustrate the ability of this synthesis to scale up to 10s of grams and the cost-effectiveness of raw materials for HAP and Fe. To enable the magnetic property of the HAPs, (3-aminopropyl)triethoxysilane (APTES)-functionalized HAP bonded with ~10-nm-sized iron oxide nanoparticles (IONPs). The IONPs had a citric acid ligand via hydrogen bonding between

the amino group of APTES in HAP and the carboxy group in the citric acid ligand of the IONPs. The HR-TEM image in the second step in Fig. 1a shows the IONP-decorated surface of a HAP nanorod building block. Subsequently, the HAP/IONPs composites are annealed at 500ºC for 2 h under a reductive atmosphere to 1) form HAP/Fe composites with ~9.5-nm-sized pure Fe nanoparticles (Supplementary Fig. 3) and 2) remove the existing polymer ligand for improved magnetic property and surface area. As shown in Supplementary Fig. 4, the magnetic intensity of HAP/Fe is larger than that of HAP/IONPs, and these data help to better understand the magnetic properties of HAP/Fe composites taken by using a permanent Nd magnet, shown in the third step in Fig. 1a. Low- and high-resolution TEM images (Fig. 1b and inset image of Fig. 1b) also show that Fe nanoparticles are bond to hollow HAP microspheres. The fast Fourier transform (FFT) patterns of HAP/Fe, which correspond to the magnified inset image of Fig. 1b, show the (300) plane of HAP and (110) plane of Fe. Energy-dispersive X-ray spectroscopy (EDX) elements-mapping images reveal that Fe nanoparticles uniformly decorate the entire HAP particle (Fig. 1c and Supplementary Fig. 5). The X-ray diffraction (XRD) analysis of HAP, HAP/IONPs, and HAP/Fe in Fig. 1d also confirm the successful formation of Fe after reduction annealing, with the obtained powder showing a sharp Fe peak at 44.7º corresponding to the (110) plane of Fe metal in the XRD pattern of HAP/Fe. As shown in Supplementary Fig. 6, the XRD patterns of HAP/Fe composites had no noticeable phase change after long-term exposure to both air and DMF, indicating that the HAP/Fe composite is quite stable for use as the adsorbent.

The results of Brunauer-Emmett-Teller (BET) and Barrett-Joyner-Halenda (BJH) analysis in Fig. 1e and Table 1 show the surface properties of HAP, HAP/IONPs, and HAP/Fe composites. The HAP/Fe composite has the highest BET surface area and BJH total pore volume, corresponding to 152.9 m^2 g^{-1} and 0.514 cm^3 g^{-1}, respectively, which is larger than those of the control HAPs. This improving phenomenon of surface properties can be described by the process of attachment of the IONPs with bulky functional polymer ligands and selective removal of the polymer ligands. The inset in Fig. 1e displays a significant change in pore distribution during the IONPs decoration of the HAP surface, which is the drastic decrease of small pores, while an increase in the number of large pores. This implies that the nano-sized pores (~10 nm) of HAPs act as effective reaction sites to ligands of IONPs, and simultaneously, their sizeable functional polymer groups form large pores. After removing ligands through reduction annealing, the nano-

sized pores are almost recovered, indicating that the decorated Fe nanoparticles have a negligible effect on the surface area of their HAP host.

Fig. 1f presents the Pb-adsorbing property of prepared HAP, HAP/IONPs, and HAP/Fe composites through a comparison of the Pb concentrations of 2 mM PbI_2-DMF solution before and after filtration with 50 mg of particles. As expected, improvement in the Pb-adsorption property via control of the surface electrostatic property after Fe-decorating the HAP/Fe composite yielded the highest adsorbing property compared to those of others. We further performed a Pb adsorption test using HAP and HAP/Fe under varied conditions, such as the type of solvent, amount of adsorbent, and adsorption time to: confirm the tendency for reactivity between prepared adsorbents and Pb^{2+} ions, and establish the best adsorption conditions (see Supplementary Fig. 7-8). Consequently, we determined the experimental conditions for further Pb removal/separation, and the best effect for Pb removal/adsorption was confirmed on DMF (among DMF, DMSO, and NMP), 70 mg of HAP/Fe, and after 30 min. Furthermore, HAP and HAP/Fe show excellent adsorption properties in aqueous solution (water) and nonaqueous aprotic polar-based solution (DMF, in this study), despite the Pb-adsorption mechanism being changed from ion exchange to electrostatic interaction (see Supplementary Fig. 9 for details on adsorption kinetics and absorption mechanisms). This means that the DMF molecule does not affect the adsorption of Pb ion at the adsorbent's surface. This is supported by reaction modeling between the adsorbent and Pb at the surface of adsorbents (HAP or HAP/Fe) with DMF condition. In our density functional theory (DFT) calculations, DMF molecules preferentially interact with Ca atoms on the HAP surface via O atoms, whereas metal atoms (Pb and Fe) form bonds with O atoms on the surface. Different adsorption mechanisms of DMF and metal atoms are consistent with the excellent adsorption of Pb in both water and DMF solutions in experiments.

Origin of improved Pb adsorption properties of Fe decorated HAP

The surface charge of absorbents plays an important role in Pb^{2+} ion absorption. In particular, absorbents with a negative surface charge show higher interaction with Pb^{2+} ions. Thus, to understand the impact of Fe on the surface charge of HAPs, we analyzed the electrochemical properties of HAP/Fe using X-ray photoelectron spectroscopy (XPS) and zeta

potentials. XPS spectra in Fig. 2a display the Fe 2*p* peaks for HAP/Fe, HAP/IONPs, and HAP. After reduction annealing at 500ºC, HAP/Fe exhibits a distinct Fe(0) peak at 706 eV, which is well-matched with the XRD results of transformed Fe in HAP/Fe. We also confirmed that the transformed Fe in HAP/Fe has many peaks between 710~730 eV, corresponding to Fe^{2+} and Fe^{3+}. Furthermore, the O 1*s* peak of HAP/Fe has been shifted toward higher bonding energies in the XPS spectra of O 1*s* of HAP/Fe (see the upper panel in Supplementary Fig. 10). In addition, as shown in Supplementary Fig. 11, the shift of the (002) plane of the HAP peak to a higher angle was observed for the HAP/Fe samples whereas there was no change for XRD peaks of pure HAP, reduction-annealed HAP without IONPs (HAP_RA), and HAP/IONPs. This means that the lattice constant of HAP was decreased due to the doping of Fe^{2+} or Fe^{3+}, which had smaller ionic radii than the Ca^{2+} at the HAP surface.[26] Even though the phase of Fe nanoparticles on HAP/Fe mainly remains as Fe metals, the Fe^{2+}/Fe^{3+} ions on the HAP surface have bonded with the neighboring oxygen in a form of Ca-O-Fe as doping.[26]

The zeta potential measurement was used to explore the surface charge of samples in Fig. 2b. The zeta potential of HAP, HAP/IONPs, and HAP/Fe is −22.28, −16.17, and −27.98 mV, respectively. Typically, HAP has a negatively charged oxygen surface from phosphate, which leads to a negative surface charge in neutral pH.[22] Because the isoelectric point of IONPs is higher than 8, the zeta potential of HAP/IONPs is more strongly positive than that of HAPs.[27] Unlike HAP/IONPs, the incorporated Fe alters the surface potential due to its imbalanced charge distribution, leading to a stronger negative potential shift than that of pristine HAP.[28,29] As shown in Fig. 2c, the zeta potential value of HAP/Fe is lower than that of HAP in the entire pH range from 3 to 10. Based on the results of electrostatic surface properties of synthetic particles, the difference in ability of cation attraction between HAP and HAP/Fe is expressed in Fig. 2d. The schematic diagrams in Fig. 2d represent the change in the electrical double layer (EDL), with a more compact Stern layer (the first layer of EDL) of cations strongly bound to a negatively charged surface layer after Fe decoration on the HAP surface. A more strongly negatively charged HAP/Fe particle enhances the electrostatic interaction with a positively charged Pb^{2+} cation. That is, bonded Fe on the surface of HAPs would enable an increase in the adsorption density of Pb^{+} ions with higher ionic strength. Consequently, a higher density of Pb^{+} ions surrounding the surface leads to the formation of a narrower slipping plane, in which the electrostatic force is drastically reduced. This means that a higher concentration of positively

charged Pb^{2+} ions would be adsorbed with a small screening length on a strongly negatively charged HAP/Fe surface.

To confirm our experimental hypothesis about Fe effects on the surface charge of HAP, we explored surface modeling of HAP and HAP/Fe with Pb via first-principles DFT simulations. Before simulating Pb adsorption with HAP and HAP/Fe, we calculated the preferential adsorption site of Pb. As shown in Supplementary Fig. 12 and Table 2, Pb shows a strong preference for three Pb-O bonds, and this is well-matched to the XPS results (Supplementary Fig. 9c). When an additional Pb atom is incorporated near an adsorbed Pb atom, the second Pb atom also forms two or three Pb-O bonds. The stabilized distance between these neighboring Pb atoms is 4.4 Å. We find an effect on the absorption in Fe-incorporated HAP, owing to a chemical interaction between Pb and Fe. In the presence of Fe, the stabilized distance between these Pb atoms is 3.2 Å, as shown in Fig. 2e and 2f. A higher density of Pb atoms could be adsorbed on the HAP/Fe surface because of the closely packed Pb atoms, which can explain the enhanced Pb-removal property of the HAP/Fe composite. However, if Fe atoms cover a large portion of the HAP surface, the absorbance of Pb should be impeded because Fe-O bonds are stronger than Pb-O bonds.

Fe decoration effects on HAP for Pb capturability

We validified the correlation between the enhanced surface property and reduced adsorption active site after Fe-decorating through examining the Pb-adsorption property of HAP/Fe with different Fe concentration. Fig. 3a presents the Pb concentration after filtration using HAP/Fe with different Fe amounts from 0 to 15 wt%. The Pb removal of HAP/Fe increased as the amount of Fe loading increased, until 10 wt%. Even the Fe has a negligible Pb-adsorption property. Above 10 wt% of Fe loading, the amount of adsorbed Pb decreases. This tendency supports the results of theoretical modeling of the Fe effect. Fig. 3b illustrates how Pb atoms would be distributed when adsorbed onto a HAP or HAP/Fe surface. In our DFT calculations, we consistently found that a single Pb atom forms three Pb-O bonds. An additional Pb atom can be adsorbed in the vicinity of the pre-adsorbed Pb atom, but it is not thermodynamically favored, indicating that Pb atoms will be adsorbed uniformly on the HAP surface. A single Fe atom, on the other hand, was found to form four Fe-O bonds on the HAP

surface. When we located an additional Pb atom near the adsorbed Fe atom, the Pb atom can make various configurations with one, two, or three Pb-O bond(s). Such structural diversity enables adsorption of two Pb atoms near a Fe atom with a short distance between them, as shown in Fig. 2f, resulting in higher adsorption of Pb atoms on the HAP/Fe surface than on the bare HAP surface.

Fig. 3c shows the Pb-adsorption properties of HAP/Fe in PbI_2–DMF and perovskite precursor solution, which is a representative case of Pb-containing nonaqueous solution waste. To determine the case-experimental condition, we investigated Pb adsorption using various conditions, such as Pb concentration and amount of adsorbent (see Supplementary Fig. 7), and the most effective condition for Pb removal/adsorption was confirmed on DMF (among DMF, DMSO, and NMP), 70 mg of HAP/Fe, and after 30 min. After a 30-min reaction between 70 mg of each adsorbent (PbI_2–DMF and perovskite precursor solution under continuous shaking), the residual Pb concentration falls to below 15 ppb in both solutions, which means it is a safe solvent based on the EPA rule.[30,31] Supplementary Video 1 shows the typical protocol for Pb removal/separation, including Pb adsorption and Pb separation from a solvent using HAP/Fe composite. Further, Pb adsorption by HAP/Fe in nonaqueous solvents has enormous potential to be extended to the removal of other toxic heavy metals, such as Sn^{2+}, which is widely used in narrow-bandgap perovskite materials.[32] Thus, we applied the HAP/Fe adsorbent for Sn^{2+} removal (20 mL of 2 mM of SnI_2 in DMF), and HAP/Fe shows an excellent absorbing property, as shown in Supplementary Fig. 13.

Demonstration of the Pb management system

Fig. 4 shows our demonstrated Pb management system and covers the complete steps related to PCSs. We already reported on the recycling process of the substrate from degraded devices, as illustrated in step 1 and step 2 in Fig. 4a, using the selective dissolving approach.[8] Step 3 in Fig. 4a shows our proposed Pb purifying and recycling process using HAP/Fe composite. To use the magnetic properties of HAP/Fe in real Pb-containing pollutants, an electromagnetic coil-wrapped purifying system is devised, as shown in Supplementary Fig. 14. The *pseudo*-Pb-pollutants were prepared by dissolving 20 pieces of real perovskite solar modules with a 16-cm^2 area in 20 mL of DMF containing metal electrodes, hole-transport molecules, and

numerous elements from perovskite compositions. The HAP/Fe composite and *pseudo*-Pb-pollutant are placed together into an electromagnetic coil-wrapped bottle and are then shaken to adsorb the Pb. After completing the Pb adsorption, we applied an electromagnetic field across the bottle, and Pb-adsorbed HAP/Fe composites were attached to the wall of the container. Pb-separated solvents flowed out from this bottle and a purified solvent that meets EPA regulations on Pb emissions (below 15 ppb), from 4,000 ppb in the initial *pseudo*-Pb-pollutant, as shown in Fig. 4b.[30] Furthermore, to realize a zero Pb-pollutant policy in the PSC market, we tested the feasibility of recycling Pb from collected Pb-adsorbed HAP/Fe composites by reprecipitating the PbI_2, which is an essential raw material for perovskite. In general, HAP particles can be dissolved in an H_2O-based solution with pH values less than 2;[22] in contrast, PbI_2 has low solubility in H_2O regardless of the pH. To use these differences of solubilities, we dispersed Pb-adsorbed HAP/Fe into 20 mL of 0.5 M HNO_3 acidic solution. Then, 1 M of KI solution was poured into the solution to recrystallize PbI_2, as shown in step 4 in Fig. 4a. Consequently, we have reached the 99.97% of Pb recycling yield (Fig. 4c). The obtained PbI_2 powder is confirmed using the photo images in step 4 of Fig. 4a and XRD patterns of obtained PbI_2 in Supplementary Fig. 15, respectively. Fig. 4d and Supplementary Table 3 informed the quality of collected PbI_2 as a perovskite raw material with similar device performance as commercially available PbI_2. The performance of the device has a strong correlation with the quality of the raw material. Therefore, recycled PbI_2 is comparable in quality to commercial PbI_2; thus, our study enables a zero-lead-emission route for future perovskite technologies.

Conclusions

In summary, we successfully synthesized a novel Pb adsorbent, a HAP/Fe composite with enhanced Pb uptake capacity and magnetism, by incorporating Fe. The prepared HAP/Fe composites demonstrate a reinforced Pb-adsorption property that meets EPA regulations on Pb emissions (below 15 ppb) and an expedient and easy collection of Pb-adsorbed HAP/Fe composites from a purified DMF. Our experimental and theoretical investigations cross-verified that the embodied Fe induced a shift to a stronger negative charge and improved the electrostatic interaction at the surface of HAP by charge delocalization, consequently enhancing the Pb-adsorption property. Furthermore, the reinforced Pb adsorption of HAP/Fe has led to the demonstration of a complete Pb management system (including removal and recycling of Pb^{2+} ions) during the entire PSC fabrication process with a 99.97% Pb recycling yield. Our approach paves a way for PSC manufacturing with zero Pb emission, by extension, provides the methodology for recycling and managing lead from waste devices to allay concerns on Pb-related environmental issues. Moreover, this study demonstrates the potentials of utilizing the economical and bio- and environment-friendly adsorbents for heavy metal management in pollutants including the organic solvents that have been used conventionally in the industry.

Methods

Materials. Poly(sodium 4-styrene sulfonate) (PSS, 30 wt.% solution in water, Sigma-Aldrich, MW 70,000), calcium nitrate tetrahydrate ($Ca(NO_3)_2{\cdot}4H_2O$, 99%, Sigma-Aldrich), sodium carbonate (Na_2CO_3, 99%, Sigma-Aldrich), disodium hydrogen phosphate (Na_2HPO_4, 99%, Sigma-Aldrich), (3-aminopropyl)triethoxysilane (APTES, $H_2N(CH_2)_3Si(OC_2H_5)_3$), citric acid ($C_6H_8O_7$, 99%, Sigma-Aldrich), *N*-*N* dimethylformamide (DMF, Sigma-Aldrich), dimethyl sulfoxide (DMSO, Sigma-Aldrich), lead nitrate ($Pb(NO_3)_2$, 99%, Sigma-Aldrich), and lead iodine (PbI_2, 99%, Sigma-Aldrich) were used as received, without further purification.

Synthesis of hollow hydroxyapatite spheres. Hollow hydroxyapatite spheres (HAP) were synthesized using the Kirkendall effect assisted ion-exchange method with a $CaCO_3$ template prepared using a fast precipitation method.[24,25] Typically, for $CaCO_3$ spheres, 15 mmol $Ca(NO_3)_2$ and Na_2CO_3 are dissolved in 600 mL of PSS with a concentration of 25 g L^{-1} and 120 mL deionized water, respectively. Then, the Na_2CO_3 solution is added to $Ca(NO_3)_2$ and PSS mixed solution with constant stirring for 30 min. After collecting the white precipitations via centrifugation, the powder is washed several times with deionized water. To convert the $CaCO_3$ spheres into HAPs, 500 mL of 0.5 M of Na_2HPO_4 were added into the obtained $CaCO_3$ spheres dispersed in 500 mL of water. The pH of the mixture was adjusted to 11.0 using ammonia solution, and it was poured into a glass bottle, sealed, and maintained at 120°C for 4 h. Afterward, the resultant powder was collected via centrifugation and washed several times with deionized water and ethanol, then dried at 60°C for 2 h in a vacuum oven.

Fe nanoparticles surface-decorating on HAPs for magnetic-property functionalizing. To give magnetic properties to HAPs, iron oxide nanoparticles (IONPs) were attached to the surface of HAPs. Surface functionalization was conducted on the HAPs and IONPs. For the amino-functionalized HAPs, 100 mg of HAPs were put into 100 mL of APTES solution. After that, the HAPs-dispersed APTES solution was heated at 70°C under vigorous stirring for 3 h to amino-functionalize the HAP surface. The resulting composites were washed several times with ethanol via centrifugation. For carboxy-functionalized IONPs (COOH-IONPs), a dispersion of 10 mg of the IONPs in 1 mL of chloroform were added to 10 mL of citric acid/DMSO solution with a concentration of 20 mg mL^{-1}, and the mixture was heated at 70°C for 3 h with vigorous stirring. After washing the COOH-IONPs using ethanol, the nanoparticles were dispersed in ethanol with a concentration of 10 mg mL^{-1}. Afterward, we mixed the COOH-IONPs and amino-functionalized HAP with different weight ratio for 3 h at room temperature. In general, to attach the COOH-IONPs on amino-functionalized HAP, 1 g of amino-terminated HAP powder was added to 10 mL of COOH-IONPs solution (10 mg mL^{-1}). The resultant magnetic composites were separated using a permanent Nd magnet. The prepared HAP/IONPs composites were annealed at 500°C under a reductive atmosphere with 5 v/v% of H_2/N_2 mixed gas to take away the functionalized polymer ligand and form HAP/Fe composites.

Materials characterization. The morphology and size of the particles were characterized using a field-emission scanning electron microscope (FESEM, JSM-7600F, JEOL) and a high-resolution transmission electron microscope (HR-TEM, JEM-3010, JEOL). Crystallographic characterization was conducted using X-ray diffraction analysis (XRD, Bruker advanced D8, λ = 1.5406 Å). The surface area and pore size distribution of samples were determined using Brunauer-Emmett-Teller (BET) and Barrett-Joyner-Halenda (BJH) analysis (SA3100, Berckman Coulter). The binding energies of the elements for the surface of the samples were measured using X-ray photoelectron spectroscopy (XPS, ESCA 2000, VG Microtech). The surface charge of the samples was estimated using a zeta-potential assay. The zeta potentials of samples were characterized using a zetasizer Nano Z90 potential analyzer (Malvern). Magnetic measurements for magnetization *vs* magnetic field (M-H) curves were analyzed using a vibrating sample magnetometer (VSM, MPMS3-Evercool, Quantum Design). The M-H loops were carried out in a field sweep from −50,000 to +50,000 Oe at 300 K.

Investigation of Pb adsorbability. Investigation of Pb-ion adsorbability was performed at room temperature by shaking a series of bottles at predetermined times using a shaker (SHR-1D, Wiseshake) at 120 rpm. Each bottle contained the desired quantity of the composites in a predetermined concentration of lead ion solution. $Pb(NO_3)_2$ and PbI_2 were used for the water and aprotic polar solvent (i.e., DMF) batch adsorption experiments, respectively. After the Pb-ion adsorption process, HAP samples were separated by centrifuging at 8000 rpm for 10 min, and the HAP/IONPs and HAP/Fe samples were separated using a permanent Nd magnet. The residual Pb concentration in the solution was measured through inductively coupled plasma–mass spectrometry (ICP-MS, Agilent 7500). The percent removal of Pb ion from the solution was determined using the following equation:

$$\text{Removal } \% = \frac{C_0 - C_f}{C_0} \times 100$$

where C_0 is the initial concentration of a Pb ion, and C_f is the final concentration of the Pb ion.

Materials modeling. To provide an understanding of the adsorption at the atomistic level, we performed first-principles density functional theory (DFT) calculations and investigated the adsorption properties of Pb and Fe ions on the [010] HAP surface. We used the generalized gradient approximation (GGA) parameterized by Perdew, Burke, and Ernzerhof[33] and the projector-augmented wave (PAW) method,[34] implemented in the Vienna ab initio simulation package (VASP) code.[35] For a better description of the dispersion interaction, the DFT-D2 method proposed by Grimme was used (Grimme, 2006).[36] A higher-energy cutoff of 500 eV was used to optimize the bulk lattice constants. The optimized lattice constants were 9.49 Å and 6.84 Å, comparable to the experimental values of 9.42 Å and 6.89 Å.[37] For the slab calculations, an energy cutoff of 400 eV was used throughout the calculations. Spin-polarized calculations were done to account for spins of the Fe ions. The thickness of the vacuum and slab were about 14 and 11 Å, respectively. While atoms at one surface were fully relaxed, atoms at the other surface

were frozen to remove interaction between the surfaces. Considering the strong P-O bonds, we broke only Ca-O bonds to generate a surface model. A flat plateau of the electrostatic potential in the vacuum region was obtained, indicating the absence of a long-range electric dipole.

Pb removal/separation pilot equipment. To address the use possibility of HAP/Fe for a continuous magnetic separation system, we fabricated Pb-removal pilot equipment, including electromagnetic coils, a magnetic controller, and a glass bottle with a stopcock. First, 250 mg of HAP/Fe powder were added to 70 mL of 2 mM PbI_2/DMF solution. The Pb adsorption was performed using pilot equipment, switching the electromagnetic field on and off several times to give a chance for a reaction between the HAP/Fe and Pb ions, instead of shaking the mixture bottle. After the reaction, the HAP/Fe particles were attracted by the generated electromagnetic field, and the Pb-free solution was dispensed from the burette.

Recycling of PbI_2 from the Pb-adsorbed HAP/Fe. The 1 g of Pb-adsorbed HAP/Fe was dissolved in 20 mL of pH 2 solution. In this study, we prepared a 0.5 M HNO_3 solution with a pH 2. The HAP/Fe composite was quickly dissolved in this solution within a few minutes. Afterward, a KI (1 M) solution was added to the Pb-ions-included solution until no more of the yellow product was formed. The yellow PbI_2 precipitate was washed with water and methanol and collected by centrifugation. The regained PbI_2 was dried in a vacuum oven at 60°C for 3 h. Then, the dried PbI_2 powder was stored in a glovebox with an N_2 atmosphere. The recycling yield of Pb ion from adsorbed Pb on HAP/Fe composites was determined using the following equation:

$$\text{Pb recycling yield (\%)} = \frac{X_0 - X_f}{X_0} \times 100$$

where X_0 is the concentration of Pb ions in a Pb dissolved solution, and X_f is a concentration of the Pb ion after recycling.

Fabrication and characterization of perovskite solar cells using recycled PbI_2. Laser-scribed FTO-coated glass substrates were cleaned with deionized water, ethanol, and acetone. A compact TiO_2 was coated on the prepared substrates by spin-coating at 4000 rpm for 30 s, using 0.1 M titanium diisopropoxide bis(acetylacetonate) solution (75% in 2□propanol, Sigma□ Aldrich) in 1-butanol, and then baking for 5 min at 135°C. They were then annealed at 500°C for 60 min. Subsequently, a 0.04 M $TiCl_4$ water solution was used to treat the TiO_2 compact layer surface at 70°C for 20 min, followed by another heat treatment at 150°C for 30 min. For the perovskite layer, the 1.5 mmol of recycled PbI_2 were dissolved in a 1 mL mixture solution of DMF and DMSO (8:2 volume ratio) at 70°C for 30 min. The PbI_2 precursor was spin-coated on the prepared substrate at 2500 rpm for 30 s, and then a cation halide solution mixture (0.08 g of formamidinium iodide, 0.008 g of methylammonium bromide, and 0.008 g of methylammonium chloride in 1 mL 2-propanol) was dropped on the PbI_2 films, followed by quick spin-coating at 5000 rpm for 30 s. Then, the semi-transparent brown color films were heated on a hotplate at 150°C for 20 min. For the control device, we used high-purity PbI_2 powder (TCI chemicals,

99.99%, trace-metal basis for perovskite precursor), and a perovskite film was fabricated using the same method. After cooling to room temperature, hole-transport material was deposited by spin-coating at 4000 rpm for 30 s. The hole-transport material solution consists of 36 mg (2,29,7,79tetrakis(N,N-di-p-methoxyphenylamine)-9,9-spirobifluorene)-(spiro-OMeTAD), 14.4 μL 4-tert-butylpyridine, and 8.8 μL of 520 mg m L^{-1} lithium bis(trifluoromethylsulfonyl)imide acetonitrile solution dissolved in 0.5 mL of chlorobenzene. The photovoltaic properties were measured using a solar simulator (Newport Oriel Solar 3A Class AAA, 64023A) equipped with a 450-W xenon lamp (Newport 6279NS), which was calibrated using a standard Si photovoltaic cell (Rc-1000-TC-KG5-N, VLSI Standards) and a potentiostat (CHI 600D, CH Instruments). All devices were measured by masking the active area with a 0.14-cm^2 mask. J-V characteristics for all devices were measured at a voltage scan rate of 0.1 Vs^{-1}.

Data availability

The data that support the findings of this study are available within the article, its Supplementary Information file and from the corresponding author upon reasonable request. Any available information on data resources used in or produced for the paper is provided.

References

1 N. J. Jeon, *et al.* A fluorene-terminated hole-transporting material for highly efficient and stable perovskite solar cells. *Nat. Energy* **3**, 682–689 (2018).

2 W. S. Yang, *et al.* Iodide management in formamidinium-lead-halide-based perovskite layers for efficient solar cells. *Science* **356**, 1376–1379 (2017).

3 J. A. Christians, *et al.* Tailored interfaces of unencapsulated perovskite solar cells for > 1,000 hour operational stability. *Nat. Energy* **3**, 68–74 (2018).

4 Y. H. Deng, *et al.* Surfactant-controlled ink drying enables high-speed deposition of perovskite films for efficient photovoltaic modules. *Nat. Energy* **3**, 560–566 (2018).

5 M. J. Yang, *et al.* Highly efficient perovskite solar modules by scalable fabrication and interconnection optimization. *ACS Energy Lett.* **3**, 322–328 (2018).

6 D. H. Kim, J. B. Whitaker, Z. Li, M. F. A. M. van Hest, & K. Zhu. Outlook and challenges of perovskite solar cells toward terawatt-scale photovoltaic module technology. *Joule* **2**, 1437–1451 (2018).

7 A. Babayigit, A. Ethirajan, M. Muller, & B. Conings, Toxicity of organometal halide perovskite solar cells. *Nat. Mater.* **15**, 247–251 (2016).

8 B. J. Kim, *et al.* Selective dissolution of halide perovskites as a step towards recycling solar cells. *Nat. Commun.* **7,** 11735 (2016).

9 N.-G. Park, M. Grätzel, T. Miyasaka, K. Zhu, & K. Emery, Towards stable and commercially available perovskite solar cells. *Nat. Energy* **1**, 16152 (2016).

10 Abate, A. Perovskite solar cells go lead free. *Joule* **1**, 659–664 (2017).

11 J. S. Lin-Fu, Vulnerability of children to lead exposure and toxicity (second of two parts). *N. Engl. J. Med.* **289**, 1289–1293 (1973).

12 M. M. Matlock, B. S. Howerton, & D. A. Atwood, Chemical precipitation of lead from lead battery recycling plant wastewater. *Ind. Eng. Chem. Res.* **41**, 1579–1582 (2002).

13 S. Bolisetty, & R. Mezzenga*,* Amyloid-carbon hybrid membranes for universal water purification. *Nat. Nanotechnol.* **11**, 365–371 (2016).

14 A. Dabrowski, Z. Hubicki, P. Podkościelny, & E. Robens*,* Selective removal of the heavy metal ions from waters and industrial wastewaters by ion-exchange method. *Chemosphere* **56**, 91–106 (2004).

15 I. Ali, and V. K. Gupta, Advances in water treatment by adsorption technology. *Nat. Protoc.* **1**, 2661–2667 (2006).

16 J. Zhao, *et al.* Facile preparation of a self-assembled Artemia cyst shell–TiO_2–MoS_2 porous composite structure with highly efficient catalytic reduction of nitro compounds for wastewater treatment. *Nanotechnology* **31(8)***,* 085603 (2020).

17 Q. L. Yuan, *et al.* Facet-dependent selective adsorption of Mn-doped alpha-Fe_2O_3 nanocrystals toward heavy-metal ions. *Chem. Mater.* **29**, 10198–10205 (2017).

18 X. Huang, *et al.* Facile preparation of hierarchical AgNP-loaded MXene/Fe_3O_4/Polymer nanocomposites by electrospinning with enhanced catalytic performance for wastewater treatment. *ACS Omega.* **4(1)**, 1897–1906 (2019).

19 C. Wang, *et al.* Facile preparation and catalytic performance characterization of AuNPs-loaded hierarchical electrospun composite fibers by solvent vapor annealing treatment. *Colloids Surf. A* **561**, 283–291 (2019).

20 S. Bailliez, A. Nzihou, E. Bèche, & G. Flamant*,* Removal of lead (Pb) by hydroxyapatite sorbent. *Process Saf. Environ.* **82**, 175–180 (2004).

21 S. Meski, S. Ziani and H. Khireddine*,* Removal of lead ions by hydroxyapatite prepared from the egg shell. *J. Chem. Eng. Data* **55**, 3923–3928 (2010).

22 Elliott, J. C. *Structure and Chemistry of the Apatites and Other Calcium Orthophosphates*. (Elsevier, 1994).

23 N. L. Ignjatović, *et al.* Rare-earth (Gd^{3+},Yb^{3+}/Tm^{3+}, Eu^{3+}) co-doped hydroxyapatite as magnetic,

up-conversion and down-conversion materials for multimodal imaging. *Sci. Rep.* **9**, 16305 (2019).
24 W. Lai, *et al.* Hydrothermal fabrication of porous hollow hydroxyapatite microspheres for a drug delivery system. *Mat. Sci. Eng. C* **62**, 166–172 (2016).
25 Y.S. Wang, Y. X. Moo, C. Chen, P. Gunawan, & R. Xu, Fast precipitation of uniform $CaCO_3$ nanospheres and their transformation to hollow hydroxyapatite nanospheres. *J. Colloid. Interf. Sci.* **352**, 393–400 (2010).
26 S. Y. Park. *et al.* Osteoinductive superparamagnetic Fe nanocrystal/calcium phosphate heterostructured microspheres *Nanoscale* **9**, 19145–19153 (2017).
27 N. Singh. *et al.* Polydopamine modified superparamagnetic iron oxide nanoparticles as multifunctional nanocarrier for targeted prostate cancer treatment. *Nanomaterials* **9**, 138 (2019).
28 V. Iannotti, e*t al.* Fe-doping-induced magnetism in nano-hydroxyapatites. *Inorg. Chem.* **56,** 4446–44583 (2017).
29 S. Kawabata, e*t al.* Synthesis and characterization of wet chemically derived magnetite□HAP hybrid nanoparticles (The American Ceramic Society, 2010).
30 B. Hailegnaw, S. Kirmayer, E. Edri, G. Hodes, & D. Cahen, Rain on methylammonium lead iodide based perovskites: Possible environmental effects of perovskite solar cells. *J. Phys. Chem. Lett.* **6**, 1543–1547 (2015).
31 USA Environmental Protection Agency Lead Laws and Regulations; http://www2.epa.gov/lead/lead-laws-and-regulations (2015).
32 A. Babayigit, e*t al. A*ssessing the toxicity of Pb- and Sn-based perovskite solar cells in model organism Danio rerio. *Sci. Rep.* **6**, 18721 (2016).
33 J. P. Perdew, K. Burke, & M. Ernzerhof, Generalized Gradient Approximation made simple. *Phys. Rev. Lett.* **77,** 3865–3868 (1996).
34 P. E. Blöchl, Projector augmented-wave method. *Phys. Rev. B Condens. Matter.* **50,** 17953–17979 (1994).
35 G. Kresse and J. Furthmüller*,* Efficient iterative schemes for ab initio total-energy calculations using a plane-wave basis set. *Phys. Rev. B* **54,** 11169–11186 (1996).
36 S. Grimme, Semiempirical GGA-type density functional constructed with a long-range dispersion correction. *J Comput. Chem.* **27,** 1787–1799 (2006).
37 M. Markovic, B. O. Flowler and M. S. Tung, Preparation and comprehensive characterization of a calcium hydroxyapatite reference material. *J. Res. Natl. Inst. Stan.* **109,** 553–568 (2004).

Acknowledgments

This work was supported by the Global Frontier R&D Program on Center for Multiscale Energy System funded by the National Research Foundation (under contract No. 2012M3A6A7054855), the Alchemist project of the Korea Institute of Energy Technology Evaluation and Planning (KETEP) granted financial resource from the Ministry of Trade, Industry & Energy (20193091010310), and the National Research Foundation of Korea (NRF) grant funded by the Korea government (MSIP) (NRF-2018M3A6A7054855, and 2019R1F1A1064095). This research was also supported by the Defense Challengeable Future Technology Program of the Agency for Defense Development, Republic of Korea. The work at the National Renewable Energy Laboratory (NREL) was supported by the De-Risking Halide Perovskite Solar Cells program of the National Center for Photovoltaics, funded by the Office of Energy Efficiency and Renewable Energy, Solar Energy Technologies Office, U.S. Department of Energy (DOE) under Contract No. DE-AC36-08GO28308 with the Alliance for Sustainable Energy, a Limited Liability Company (LLC), and the Manager and Operator of NREL. The views expressed in the article do not necessarily represent the views of the DOE or the U.S. Government. Via our membership of the UK's HEC Materials Chemistry Consortium, which is funded by EPSRC (EP/L000202), this work used the ARCHER UK National Supercomputing Service (http://www.archer.ac.uk).

Author Contributions

H.S.J. and D.H.K. supervised this work. S.Y.P. and D.H.K. conceived the idea and designed the experiments. S.Y.P., D.H.K., and J.P. discussed the mechanism and designed the experiment and theoretical calculations. S.Y.P. carried out the synthesis and characterization of materials and the Pb-management test. S.Y.P. and H.L conducted the magnetic analysis of materials. J.P. and A.W. designed and performed the theoretical calculations. B.J.K, D.H.K., and K.Z. performed the device fabrication and analysis. S.Y.P., J.P., K.Z., D.H.K, and H.S.J. wrote the first draft of the manuscript, and all authors discussed the results and commented on the manuscript.

Conflicts of Interest

There are no conflicts to declare.

Figure Legends and Tables

Fig. 1. Synthesis of magnetic hollow HAP/Fe composite and its properties for Pb absorption. **a,** Schematic and representative images of the preparation steps of magnetic hollow HAP/Fe composites. First, hollow HAP was synthesized using the Kirkendall effect assisted anion-exchange process. The SEM image on the right is a broken hollow HAP particle. The next step is the attachment of iron oxide nanoparticles (IONPs) to the surface of HAPs via hydrogen bonding to provide magnetic activity. The TEM image shows an IONP-decorated HAP surface. To form magnetic Fe on HAPs and remove surfactants, HAP/IONPs are annealed at 500ºC for 2 h under reductive 5 v/v% H_2/N_2 atmosphere. The synthesized HAP/Fe composite can be attached to the Nd magnet, as shown in the photo. **b,** Typical TEM images of prepared HAP/Fe. The inset magnified TEM image shows a sub-10-nm Fe particle on the HAP surface, and the reduced fast Fourier transform (FFT) patterns are obtained from the inset image. **c**, EDX mapping of HAP/Fe. Scale bar, 500 nm. **d,** XRD patterns of HAP, HAP/IONPs, and HAP/Fe. **e,** N_2 adsorption−desorption isotherm and pore size distributions (insets) of HAP, HAP/IONPs, and HAP/Fe. **f,** Feasibility of uptake of Pb in PbI_2/DMF using HAP/Fe. The 50-mg HAP, HAP/IONPs, and HAP/Fe are dispersed in 20 mL of 2 mM PbI_2–DMF solution, separately.

Fig. 2. Impact of Fe incorporating on surface properties of HAP. a, XPS spectra of Fe 2*p* peaks of HAP/Fe, HAP/IONPs, and HAP. The peak at 706 eV in HAP/Fe indicates the formation of Fe metal (Fe(0)). Binding energy was calibrated to C 1*s* peak. **b,** Zeta potentials of HAP, HAP/IONPs, and HAP/Fe in DMF. **c**, pH dependence of zeta potentials for HAP/Fe and HAP. We conducted a Pb-absorption experiment in the range of the green section. **d**, Schematic diagram of surface-charge difference between HAP and HAP/Fe for charge-attraction ability. **e–f,** Density functional theory (DFT) simulation of Pb adsorption on HAP and HAP/Fe, which demonstrates a Pb-Fe-Pb interaction that can increase the surface density of Pb.

Fig. 3. Fe effects on HAP for Pb capturability. a, Concentration of Pb before and after Pb adsorption using a HAP/Fe composite with different weight percent Fe in the HAP/Fe. 20 mL of 2 mM of the PbI_2/DMF solution are used as a Pb stock-solution. Error bars represent the mean ± standard deviation. **b,** DFT simulation of Pb adsorption on the surface of HAP and HAP/Fe, which demonstrates that the number of bounded Pb ions is increased with Fe doping on the surface of HAP. **c,** Removal of the Pb element in PbI_2/DMF and typical perovskite precursor composed of PbI_2, methylammonium iodide, and DMF using HAP/Fe.

Fig. 4. Illustration of the use of HAP/Fe composite for treating a Pb-containing solution pollutant and PbI_2 regaining process after Pb removal/separation. a, Process of Pb removal/separation from Pb-containing pollutant formed during manufacturing and recycling of PSCs. Gray arrow represents a Pb-containing process, and the green arrow represents a Pb-free process. Step 1: Manufacturing PSC modules. Step 2: Substrate recycling process from degraded PSC modules via selective dissolving method. Step 3: Pb-removal process from perovskite industrial pollutant using a HAP/Fe composite and electromagnetic separating system.

Photograph of the actual electromagnetic separating system shown in Supplementary Fig. 14. Step 4: Recycling of Pb by forming PbI_2 from Pb-adsorbed HAP/Fe composite. **b,** Pb concentration after Pb removal/separation using a HAP/Fe composite and electromagnetic separating system. Twenty modules with a 16-cm^2 device area were recycled in 20 mL of DMF. **c,** The adsorbed and recycled Pb amount from 1 g of Pb-adsorbed HAP/Fe. The detailed recycling process from Pb-adsorbed HAP/Fe is described in the experimental section. **d,** Statistics of efficiencies of perovskite solar cells using commercial PbI_2 (control device, black) and recycled PbI_2 from a Pb-adsorbed HAP/Fe composite

Table 1. Surface properties of the HAP, HAP/IONPs, and HAP/Fe

	BET surface area ($m^2 g^{-1}$)	**BJH total pore volume ($cm^3 g^{-1}$)**	**Average pore size [a] (nm)**	**Zeta potential [b] (mV)**
HAP	127.4	0.424	12.3	−22.5
HAP/IONPs	42.4	0.125	27.0	−17.5
HAP/Fe	152.9	0.514	17.1	−27.6

[a] Average pore size distribution according to the BJH method.
[b] Measured zeta potential of particles dispersed in DMF solution.

Figure 1

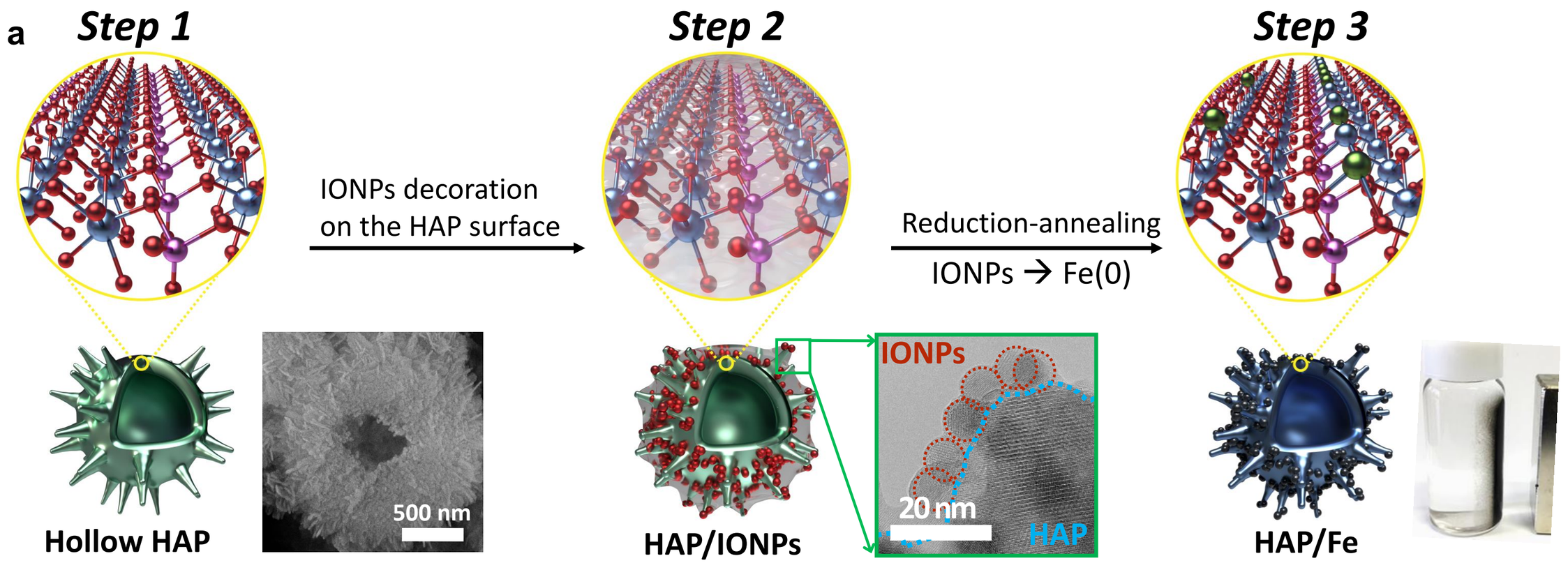
a
Step 1
Step 2
Step 3
IONPs decoration
on the HAP surface
Reduction-annealing
IONPs → Fe(0)
Hollow HAP
500 nm
HAP/IONPs
IONPs
20 nm
HAP
HAP/Fe

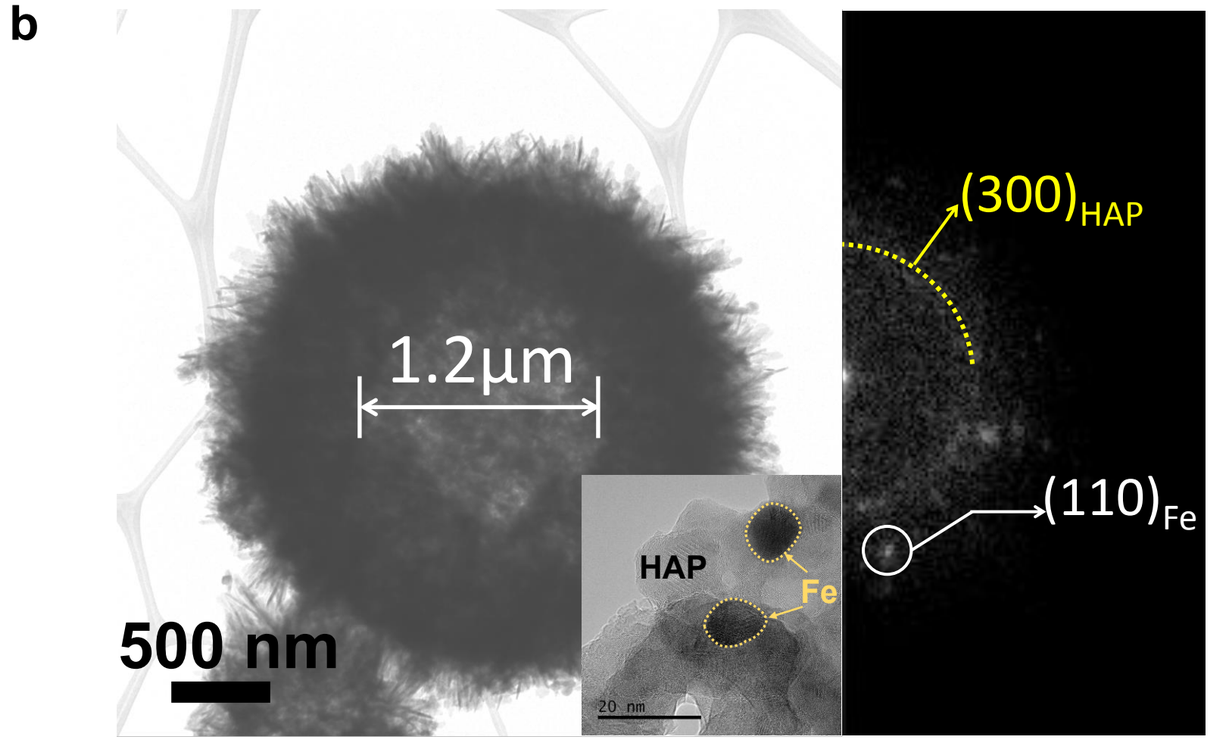
b
1.2μm
500 nm
HAP
Fe
20 nm
(300)HAP
(110)Fe

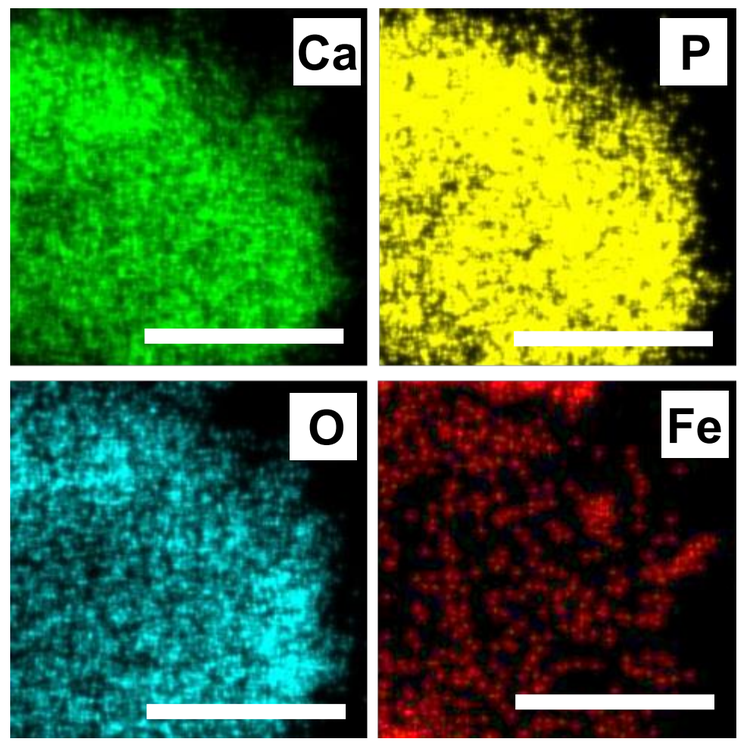
c
Ca
P
O
Fe

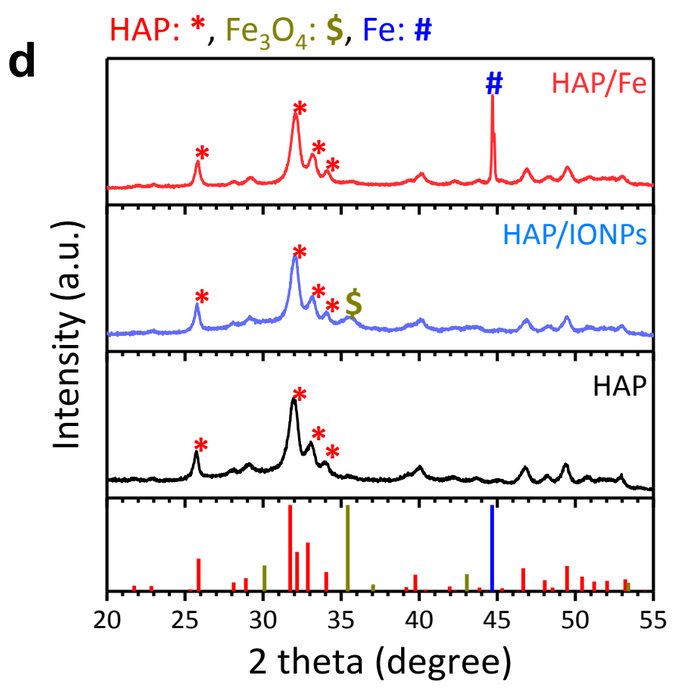
d
HAP: *, Fe3O4: $, Fe: #
HAP/Fe
HAP/IONPs
HAP
Intensity (a.u.)
2 theta (degree)

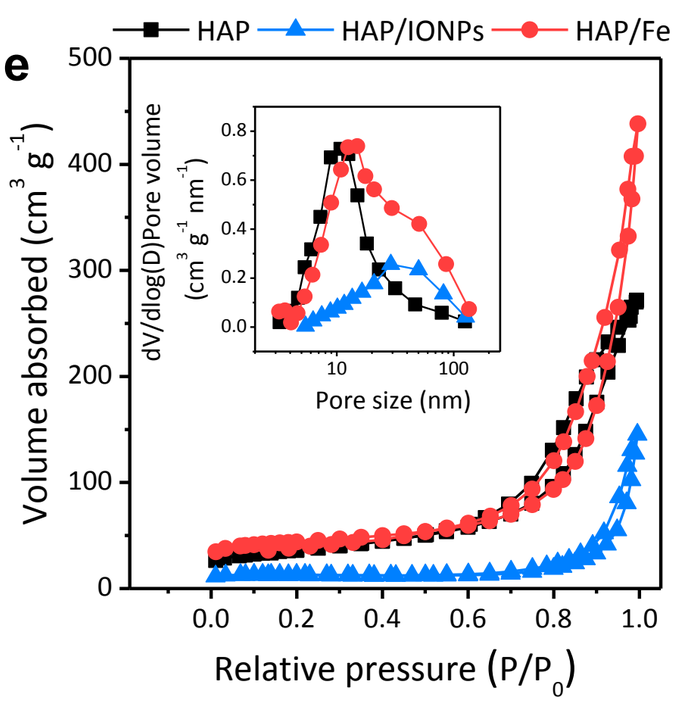
e
HAP
HAP/IONPs
HAP/Fe
Volume absorbed (cm3 g-1)
dV/dlog(D)Pore volume (cm3 g-1 nm-1)
Pore size (nm)
Relative pressure (P/P0)

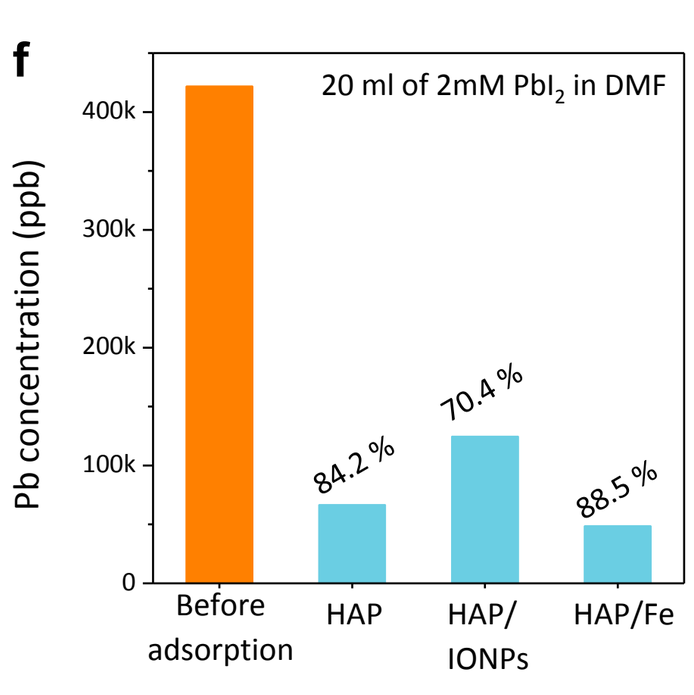
f
20 ml of 2mM PbI2 in DMF
Pb concentration (ppb)
84.2 %
70.4 %
88.5 %
Before adsorption
HAP
HAP/ IONPs
HAP/Fe

Figure 2

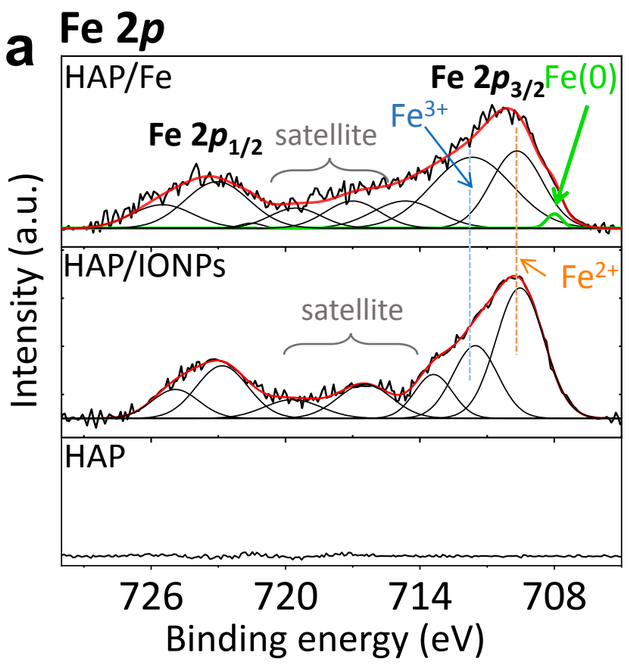
a
Fe 2p
HAP/Fe
Fe 2p3/2
Fe(0)
Fe 2p1/2
satellite
Fe3+
HAP/IONPs
Fe2+
satellite
HAP
Intensity (a.u.)
726
720
714
708
Binding energy (eV)

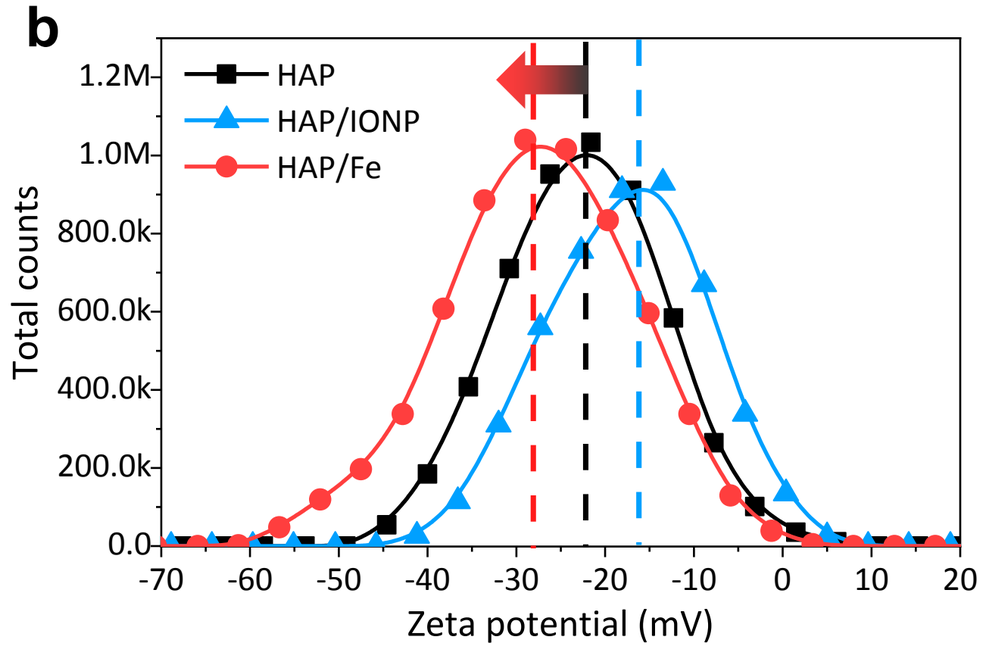
b
HAP
HAP/IONP
HAP/Fe
Total counts
1.2M
1.0M
800.0k
600.0k
400.0k
200.0k
0.0
-70
-60
-50
-40
-30
-20
-10
0
10
20
Zeta potential (mV)

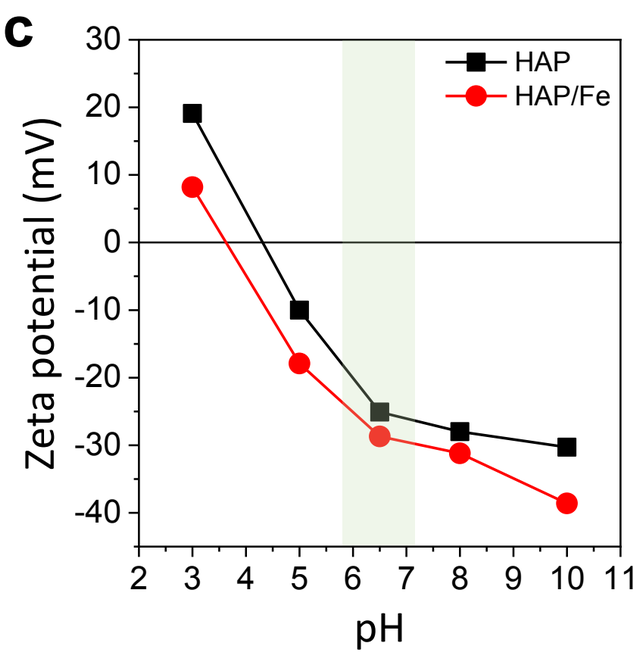
c
HAP
HAP/Fe
Zeta potential (mV)
30
20
10
0
-10
-20
-30
-40
2
3
4
5
6
7
8
9
10
11
pH

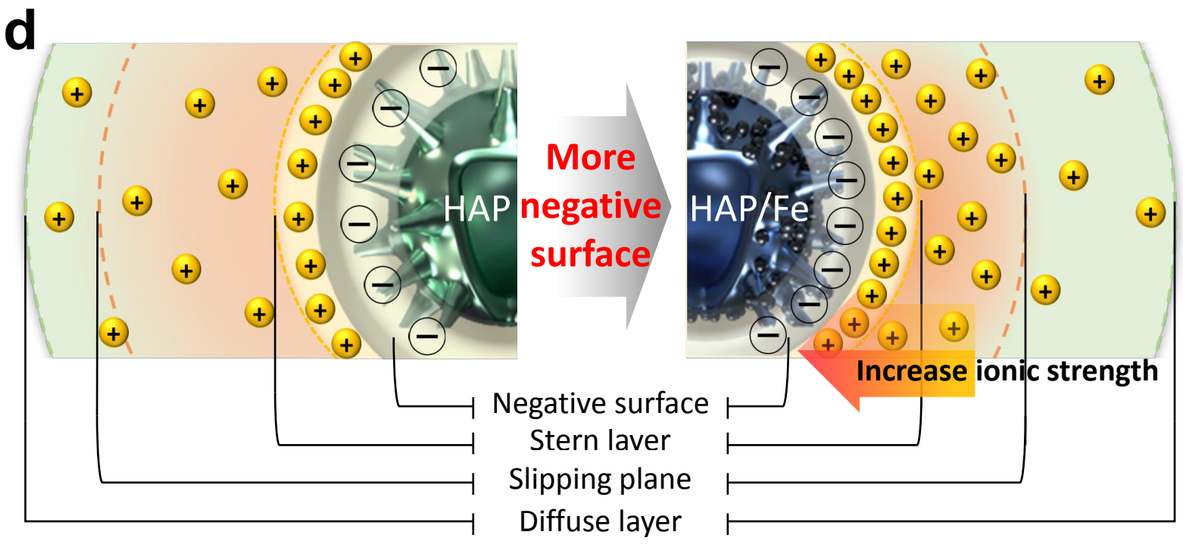
d
HAP
More negative surface
HAP/Fe
Increase ionic strength
Negative surface
Stern laver
Slipping plane
Diffuse layer

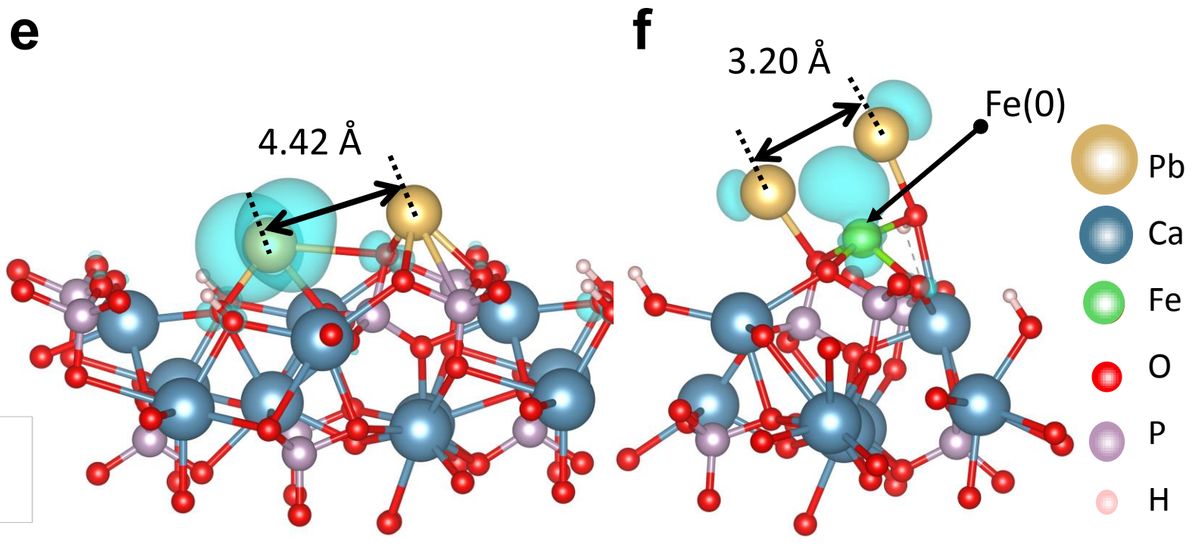
e
4.42 Å
f
3.20 Å
Fe(0)
Pb
Ca
Fe
O
P
H

Figure 3

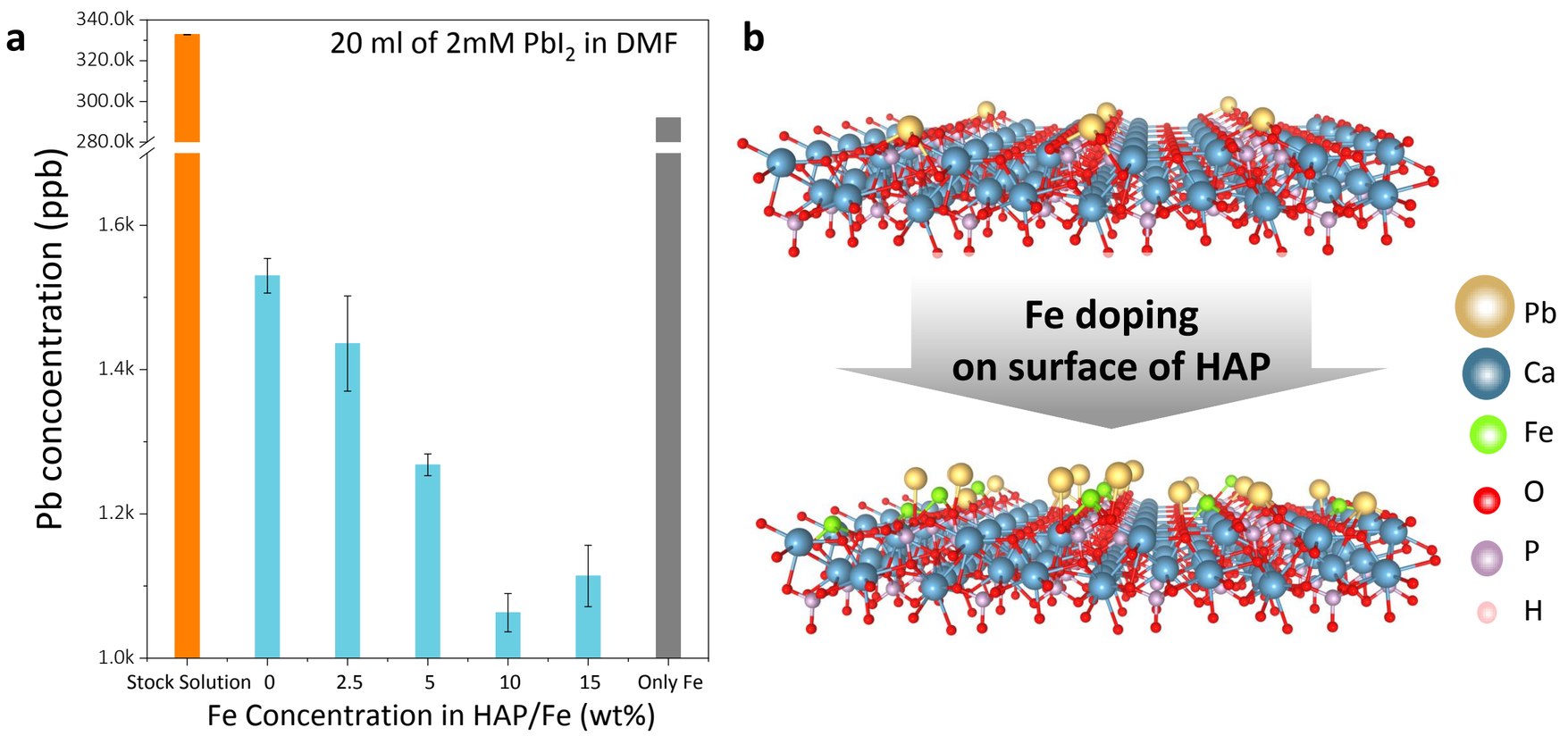
a
20 ml of 2mM PbI2 in DMF
Pb concoentration (ppb)
340.0k
320.0k
300.0k
280.0k
1.6k
1.4k
1.2k
1.0k
Stock Solution
0
2.5
5
10
15
Only Fe
Fe Concentration in HAP/Fe (wt%)
b
Fe doping
on surface of HAP
Pb
Ca
Fe
O
P
H

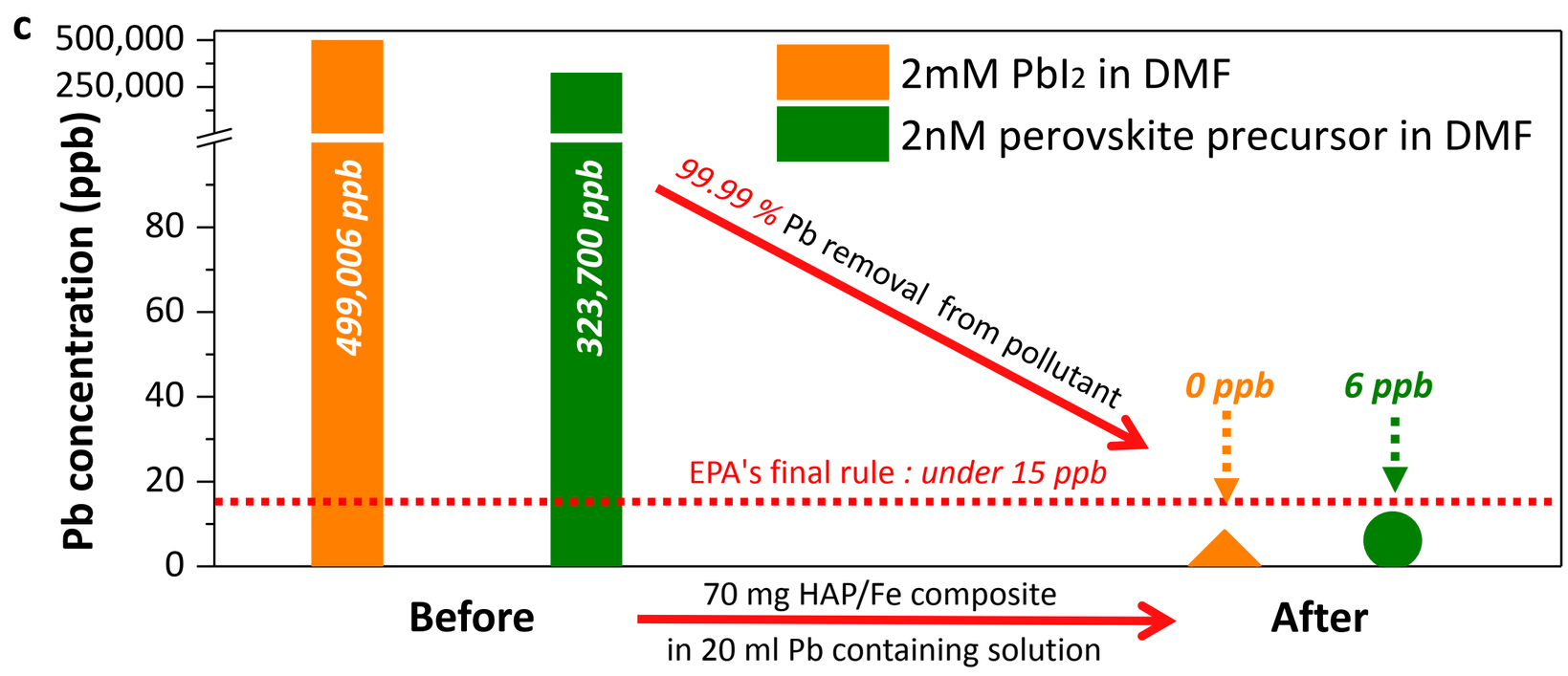
c
Pb concentration (ppb)
500,000
250,000
80
60
40
20
0
499,006 ppb
323,700 ppb
2mM PbI2 in DMF
2nM perovskite precursor in DMF
99.99 % Pb removal from pollutant
0 ppb
6 ppb
EPA's final rule : under 15 ppb
Before
70 mg HAP/Fe composite
in 20 ml Pb containing solution
After

Figure 4

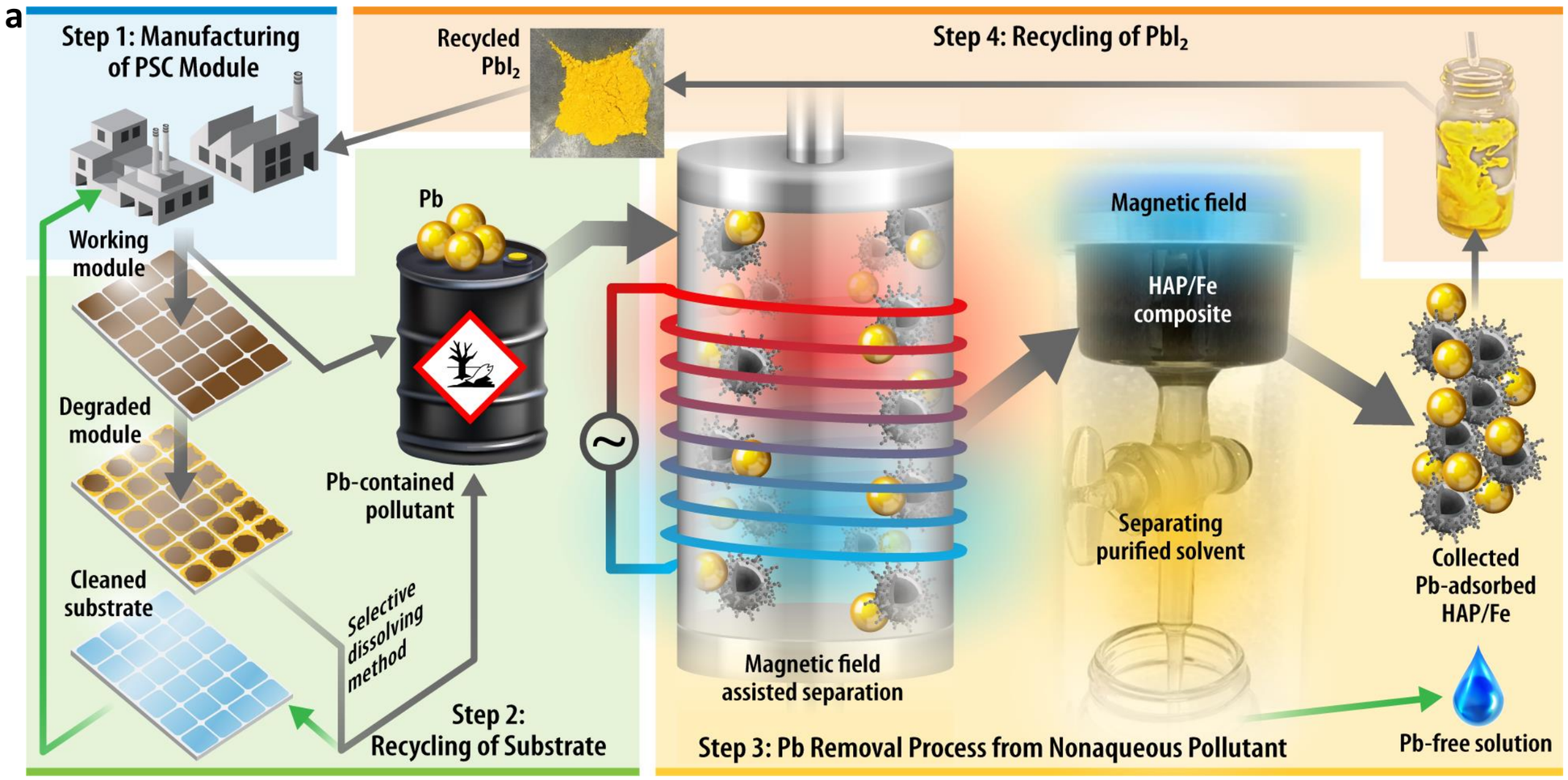
a
Step 1: Manufacturing of PSC Module
Recycled PbI_2
Step 4: Recycling of PbI_2
Working module
Degraded module
Cleaned substrate
Selective dissolving method
Step 2: Recycling of Substrate
Pb
Pb-contained pollutant
Magnetic field
HAP/Fe composite
Separating purified solvent
Collected Pb-adsorbed HAP/Fe
Magnetic field assisted separation
Step 3: Pb Removal Process from Nonaqueous Pollutant
Pb-free solution

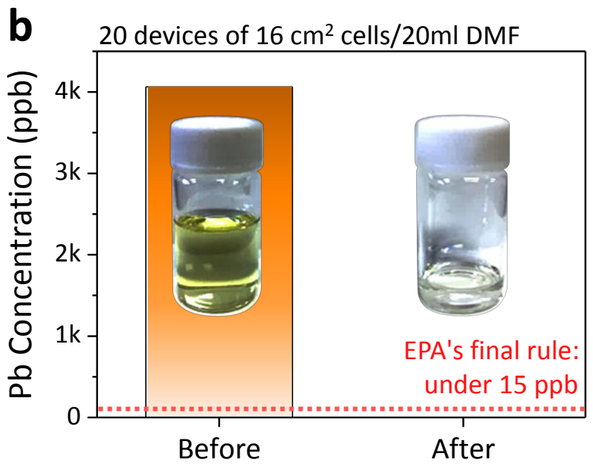
b
20 devices of 16 cm² cells/20ml DMF
Pb Concentration (ppb)
4k
3k
2k
1k
0
EPA's final rule: under 15 ppb
Before
After

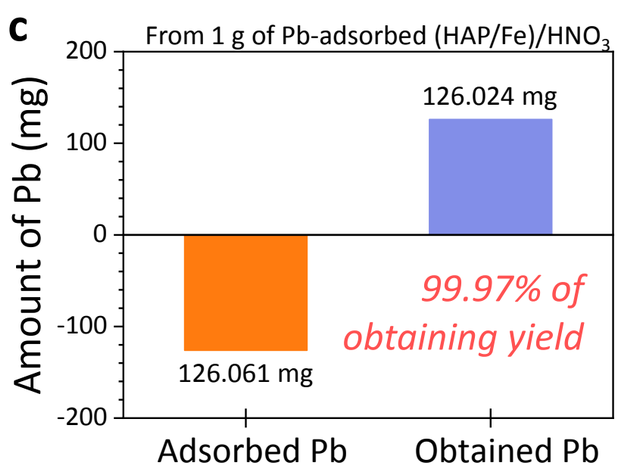
c
From 1 g of Pb-adsorbed (HAP/Fe)/HNO_3
Amount of Pb (mg)
200
100
0
-100
-200
126.024 mg
126.061 mg
99.97% of obtaining yield
Adsorbed Pb
Obtained Pb

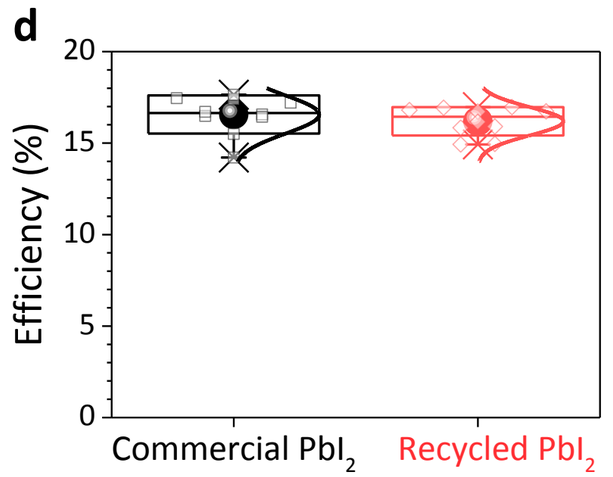
d
Efficiency (%)
20
15
10
5
0
Commercial PbI_2
Recycled PbI_2